Chapter 1

NV-NV cross-relaxation at low fields: application to magnetometry

In the last chapter we have identified a dipole-dipole relaxation mechanism within dense NV centers ensemble, and we have studied its influence in non-zero magnetic field. In this chapter we will cover the low to zero magnetic field region and see how the depolarization at low magnetic field can be used for magnetometry.

This chapter is constructed as follows: We will first describe in sec. 1.1 the physics of NV centers under low or transverse magnetic field. In sec. 1.2 we will present the different zero field depolarization causes that we have identified as well as their theoretical impact on the NV relaxation rates according to the fluctuator model. In sec. 1.3 we will confront the predictions of the fluctuator model with experiments under low and transverse magnetic field.

We will then focus on the low field depolarization magnetometry (LFDM) protocol which exploits the previously studied NV-NV CR at low magnetic field. We will start by giving a short overview of NV ensemble magnetometry in sec. 1.4 before characterizing the LFDM protocol in sec. 1.5 and comparing it to other magnetometry protocols in sec. 1.6. Finally we will give some perspectives on how to improve LFDM and on potential applications.

The results presented in this chapter are based in large part on the article [3].

1.1 NV spin Hamiltonian under low and transverse fields

We will start this chapter by studying the single NV physics under low and transverse magnetic field. On of the main difference with the previously studied regime is that the eigenstates of the Hamiltonian are no longer $\{|0\rangle, |+1\rangle, |-1\rangle\}\}$, which will then in turn modify the dipole-dipole interaction between the NV centers.

We will first describe the spin Hamiltonian of the NV center under low magnetic field and determine the dominant factors in our samples, then do the same for transverse magnetic field, and finally investigate the modification of the ODMR lineshapes in those regimes.

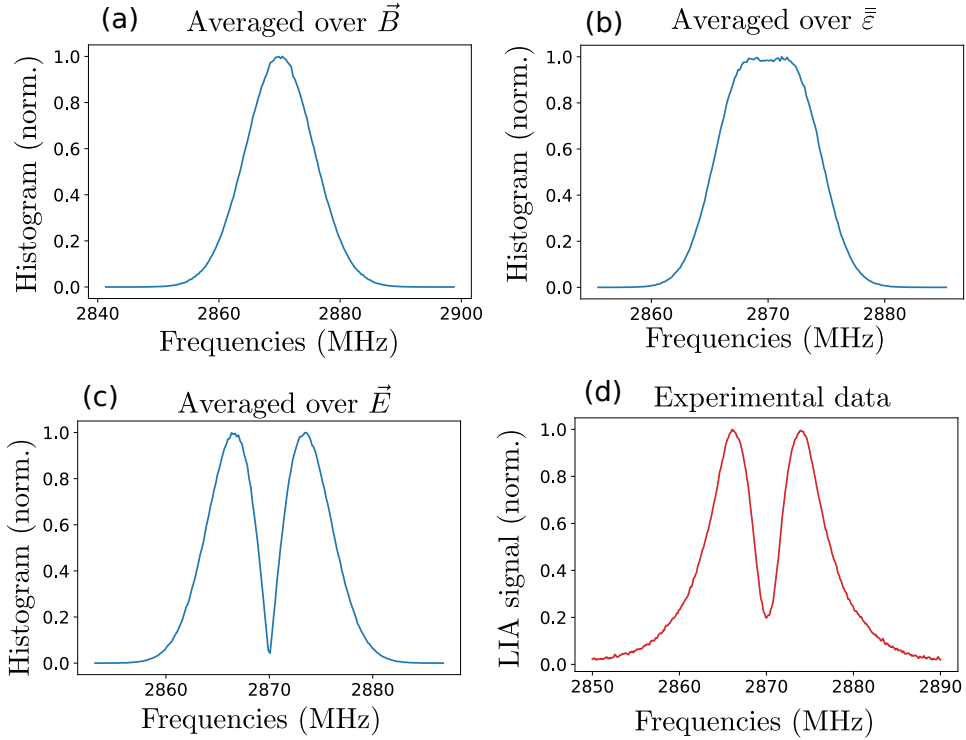### 1.1.1 NV spin Hamiltonian in zero external magnetic field

Figure 1.1: Monte-Carlo simulations of inhomogeneous zero field ODMR for different noise sources. a) Magnetic noise: each of the **B** components is sampled over a Gaussian of deviation $\sigma = 2$ G. b) Strain noise: each of the components of the strain tensor $\bar{\bar{\varepsilon}}$ is sampled over a Gaussian of deviation $\sigma = 2 \cdot 10^{-4}$. c) Electric noise: each of the **E** components is sampled over a Gaussian of deviation $\sigma = 2 \cdot 10^5$ V/cm. d) Experimental ODMR spectrum in zero external field taken on sample ADM-150-2

In the absence of a strong external magnetic field, the dominant terms of the NV spin Hamiltonian originate from local noises. These noises are: the random local magnetic fields caused by paramagnetic impurities, the local electric field caused by charged impurities, and the crystal strain [4–6].

Due to the large zero field splitting $D = 2870$ MHz between the $|0\rangle$ and $|\pm 1\rangle$ states, we will consider the $|0\rangle$ state to always be an eigenstate of the spin Hamiltonian under zero external field. The problem is then reduced to the $\{|-1\rangle, |+1\rangle\}$ subsystem.

The NV$^-$ spin Hamiltonian in the $\{|-1\rangle, |+1\rangle\}$ basis can be written as [5]:

$$\mathcal{H} = \begin{pmatrix} D - \gamma_e B_\parallel + f_\parallel(\mathbf{E}) + g_\parallel(\bar{\bar{\varepsilon}}) & f_\perp(\mathbf{E}) + g_\perp(\bar{\bar{\varepsilon}}) \\ f_\perp^*(\mathbf{E}) + g_\perp^*(\bar{\bar{\varepsilon}}) & D + \gamma_e B_\parallel + f_\parallel(\mathbf{E}) + g_\parallel(\bar{\bar{\varepsilon}}) \end{pmatrix}, \quad (1.1)$$

where $B_\parallel$ is the component of the magnetic field along the NV axis, and $f_\parallel, f_\perp, g_\perp$, and $g_\parallel$ are functions of the electric field $\mathbf{E}$ and the strain tensor $\bar{\bar{\varepsilon}}$, whose expressions are:

$$f_\parallel(\mathbf{E}) = d_\parallel E_z, \quad (1.2)$$

$$f_\perp(\mathbf{E}) = d_\perp(E_x + iE_y), \quad (1.3)$$

$$g_\parallel(\bar{\bar{\varepsilon}}) = h_{41}(\varepsilon_{xx} + \varepsilon_{yy}) + h_{43}\varepsilon_{zz}, \quad (1.4)$$

$$g_\perp(\bar{\bar{\varepsilon}}) = \frac{1}{2}\left[h_{16}(\varepsilon_{zx} + i\varepsilon_{zy}) + h_{15}\left(\frac{\varepsilon_{yy} - \varepsilon_{xx}}{2} + i\varepsilon_{xy}\right)\right], \quad (1.5)$$

where $d_\parallel = 0.35$ Hz cm/V and $d_\perp = 17$ Hz cm/V have been measured experimentally [7], and $h_{43} = 2300$ MHz, $h_{41} = -6420$ MHz, $h_{15} = 5700$ MHz and $h_{16} = 19660$ MHz were computed through DFT [5] and show reasonable agreement with experiments [8].

Fig. 1.1-a) b) and c) shows the result of Monte-Carlo simulations of the ODMR of an ensemble of NV centers for different noise sources. The simulation work as follow: one of the three possible noise source (magnetic field, electric field or strain) is sampled randomly while the two other are kept at zero. The eigenvalues of the spin Hamiltonian given in eq. 1.1 are then computed and the process is repeated 10^6 times to create the histograms shown in Fig. 1.1.

Fig. 1.1-d) shows an experimental zero-field ODMR which is typical of the samples used in this manuscript. In particular we can notice a central splitting of the spectrum. This splitting is only present in the simulation when the dominant noise is the electric field. We then conclude that the dominant noise source in our sample (in the absence of external magnetic field) is the local electric field.

The authors of [6] came to the same conclusion for the samples with dense NV ensemble that they studied by using a more sophisticated simulation model.

Given that $d_\perp \approx 50 d_\parallel$, we can consider that the dominant electric field noise comes from the transverse electric field. We will then adopt the following simplified Hamiltonian for the zero external magnetic field regime:

$$\mathcal{H} = \begin{pmatrix} D & 0 & d_\perp E_\perp^* \\ 0 & 0 & 0 \\ d_\perp E_\perp & 0 & D \end{pmatrix}, \tag{1.6}$$

whose eigenvectors are $|0\rangle$ and $|\pm\rangle$ of eigenvalues 0 and $D \pm d_\perp |E_\perp|$, where $|\pm\rangle$ are defined as:

$$|\pm\rangle = \frac{|+1\rangle \pm e^{-i\phi_E} |-1\rangle}{\sqrt{2}}, \tag{1.7}$$

where $\tan(\phi_E) = E_y / E_x$.

1.1.2 NV spin Hamiltonian under purely transverse magnetic field

We now turn to the case of a magnetic field that is orthogonal to the NV axis, i.e. $\mathbf{B} = B_x \hat{e}_x + B_y \hat{e}_y$, and more specifically to the regime where $d_\perp E_\perp < \frac{(\gamma_e B_\perp)^2}{D} << D$. In practice, this generally corresponds to 20 G $\lesssim$ B$_\perp \lesssim$ 200 G.

In this regime, the NV Hamiltonian eigenstates are similar to the case where it is dominated by the transverse electric field and can be written $\approx |0\rangle, |-\rangle, |+\rangle$[9, 10], of respective eigenvalues $\approx -\frac{(\gamma_e B_\perp)^2}{D}, D, D + \frac{(\gamma_e B_\perp)^2}{D}$, where:

$$|\pm\rangle = \frac{|+1\rangle \pm e^{-2i\phi_B} |-1\rangle}{\sqrt{2}}, \tag{1.8}$$

and $\tan(\phi_B) = B_y / B_x$.

For the case where $d_\perp E_\perp \sim \frac{(\gamma_e B_\perp)^2}{D}$ and $\phi_E \neq 2\phi_B$, the eigenstates of the Hamiltonian are still of the form $|0\rangle, |\pm\rangle$ with a relative angle ϕ in between ϕ_E and $2\phi_B$.

In conclusion, whenever the spin Hamiltonian is dominated by the local electric field or by the transverse magnetic field, we can consider that the eigenstates of the spin Hamiltonian to be $|0\rangle, |-\rangle$ and $|+\rangle$, whereas when the Hamiltonian is dominated by the longitudinal magnetic field, its eigenstates are $|0\rangle, |-1\rangle$ and $|+1\rangle$.

1.1.3 Hyperfine and inhomogeneous broadening

A consequence of the change in the Hamiltonian eigenstates from the $\{|0\rangle, |\pm 1\rangle\}$ to the $\{|0\rangle, |\pm\rangle\}$ basis is that the Hamiltonian eigenvalues are sensitive to different part of the environment. The energy of the $|\pm 1\rangle$ states depends linearly on the longitudinal magnetic field, and quadratically on the transverse electric and magnetic fields. On the contrary, the $|\pm\rangle$ states depend linearly
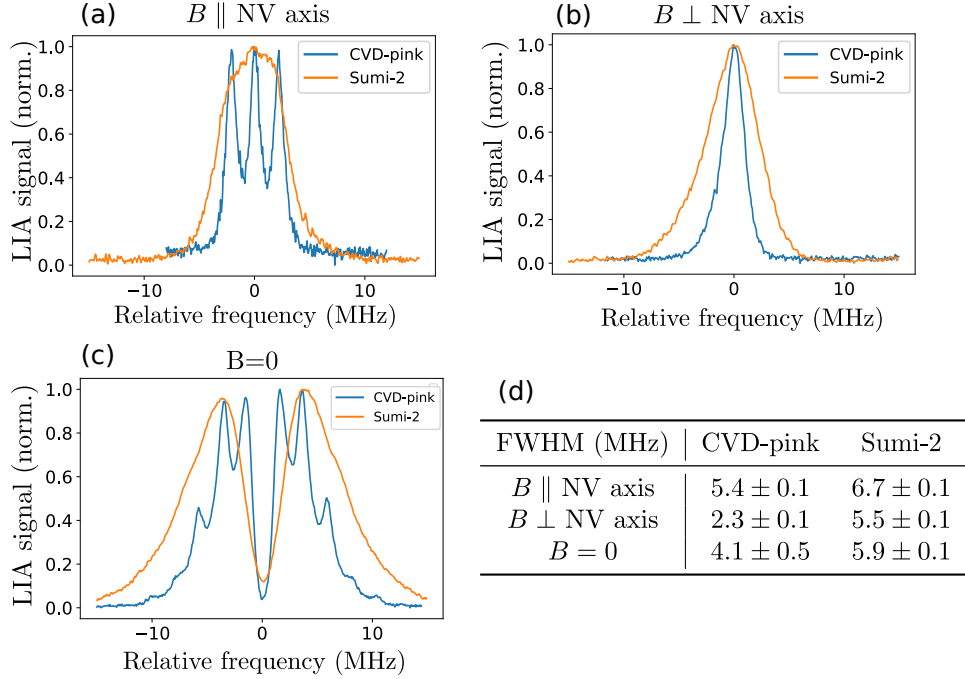
Figure 1.2: ODMR lineshapes for longitudinal, transverse and low magnetic fields on samples CVD-pink and Sumi-2. a) ODMR spectrum of a single class of NV centers for a longitudinal magnetic field ($B_\parallel \sim 100\,\mathrm{G}$). The microwave frequency is given with respect to the ODMR line central frequency. b) ODMR spectrum of a single class for a purely transverse magnetic field ($B_\perp \sim 100\,\mathrm{G}$). c) ODMR of all 4 classes for 0 external magnetic field. d) Table reporting the full width at half maximum of each ODMR line.

on the transverse electric field, and quadratically on the longitudinal and transverse magnetic field [1].

The shape of the ODMR lines (i.e. the spectral response of the spins) is therefore dominated by the magnetic noise and the hyper-fine coupling in the $\{|0\rangle, |\pm1\rangle\}$ basis, and by the electric noise in the $\{|0\rangle, |\pm\rangle\}$ basis, as we established in the previous part. Further details on the low magnetic field regime are available in [11] and on the purely transverse magnetic field regime in [9, 10].

Fig. 1.2 shows ODMR profile on two samples, CVD-pink which shows weak dipole-induced depolarization and Sumi-2 which shows strong dipole-induced depolarization, in three distinct regime: for a purely longitudinal magnetic field, for a purely transverse magnetic field, and without magnetic field. The linewidths of the spin transition [2] for both samples are reported

---

[1] The transverse magnetic field is always of second order for weak magnetic field because $D \gg \gamma B_\perp$.

[2] We consider here the full linewidth of the electronic levels, i.e. including all three

in the Table 1.2-d). In both cases, the linewidths are smaller in the $B = 0$ and $B \perp NV$ cases than in the $B \parallel NV$ case, mainly due to the modification of the hyper-fine coupling. The linewidth modification reaches up to $\sim 50\%$ for the CVD sample and $\sim 20\%$ for the HPHT one.

We are particularly interested in the spin transition linewidth since it directly impacts the dipole-dipole relaxation rate (as seen in sec. [REF]): the smaller the linewidth, the higher the dipole-dipole relaxation rate is.

To summarize this section, we have seen that (for the samples used in this chapter) the NV center spin Hamiltonian is dominated by transverse electric field at low external magnetic field, which causes a change of the Hamiltonian eigenstates from $\{|0\rangle, |\pm 1\rangle\}$ to $\{|0\rangle, |\pm\rangle\}$.

We have also seen that the spin Hamiltonian has the same eigenstates for purely transverse magnetic field than it does for low magnetic field.

Finally we have seen that this change of eigenstates occasions a modification of the spectral profile and linewidth of the spins.

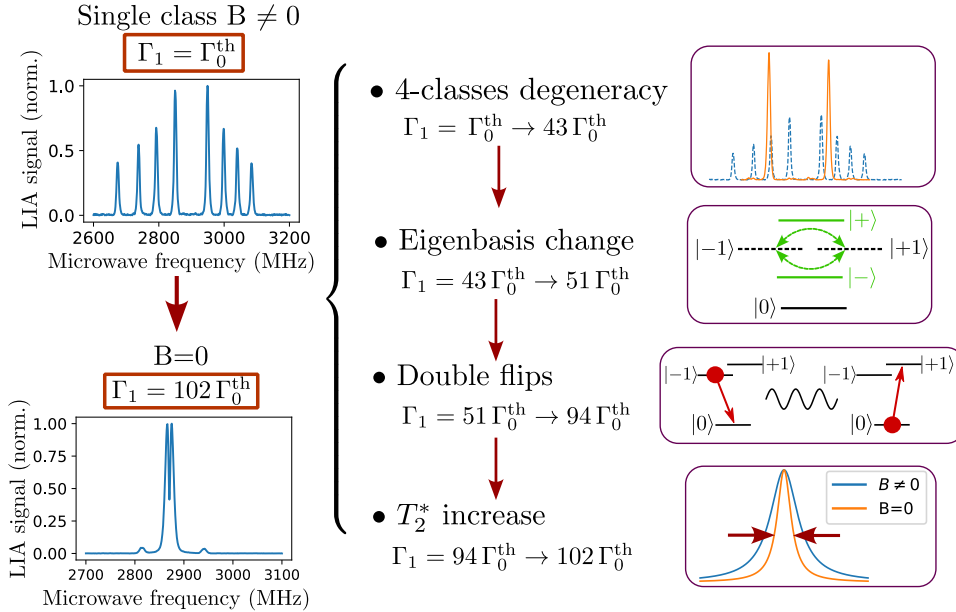## 1.2 Theory of the low field depolarization

Figure 1.3: Summary of the different depolarization effects in low magnetic field and their predicted depolarization rate. The ODMR spectra were taken on sample ADM-150-1

hyper fine levels

We will focus on this section on the mechanisms responsible for the depolarization of dense NV ensemble at low magnetic fields. We have identified four such mechanisms that lead to an increase in the resonant dipole-dipole coupling between NV and fluctuators, which in turn results in an increased spin depolarization rate.

Fig. 1.3 summarizes these four mechanisms along with the theoretical increase in the depolarization rate caused by each of them. We will detail below the physical origin of these four mechanisms and the calculations that lead to the values presented in Fig. 1.3.

We should note that the values indicated in Fig. 1.3 for the double flips and the T_2^* contributions depend on experimental parameters, while the ones for the 4-classes degeneracy and the eigenbasis change are purely based on theory.

1.2.1 Four classes degeneracy

The first and main contribution to the low field depolarization is the degeneracy between the four classes as the magnetic field decreases. Following the arguments presented in the last chapter, the degeneracy between the four classes of NV centers causes in theory an increase in the relaxation rate by a factor ~ 43. This contribution is not specific to the zero field region, as we can observe the same resonance condition when $\mathbf{B} \parallel [100]$.

1.2.2 Eigenstates modification

The modification of the Hamiltonian eigenstates discussed in sec. 1.1.1 from the eigenbasis $\{|0\rangle, |+1\rangle, |-1\rangle\}$ when $B \neq 0$ to the eigenbasis $\{|0\rangle, |+\rangle, |-\rangle\}$ when $B \sim 0$ changes the dipole-dipole interaction between the two spins.

A consequence of this change is the absence of diagonal terms in the dipole-dipole Hamiltonian written in the $\{|0\rangle, |+\rangle, |-\rangle\} \times \{|0\rangle, |+\rangle, |-\rangle\}$ basis, which explains why the NV centers states are protected from magnetic noises at low magnetic field [11].

Another consequence is a slight modification of the flip-flop rates. Once averaged over all possible orientation and position, as detailed in appendix [REF], this modification of the flip-flop rates amount for an increase of Γ_1 by about 20 % in the $\{|0\rangle, |+\rangle, |-\rangle\}$ basis compared to the $\{|0\rangle, |+1\rangle, |-1\rangle\}$ basis.

1.2.3 Double flips

The double flip processes have been previously discussed in sec. [REF] and naturally arise from the dipole-dipole Hamiltonian. The ones that we consider here couple the states $|0, \pm 1\rangle$ and $|\mp 1, 0\rangle$ (in contrast with the flip-flop which couple the states $|0, \pm 1\rangle$ and $|\pm 1, 0\rangle$). These terms are generally

not resonant because of the Zeeman splitting between the $|+1\rangle$ and $|-1\rangle$ states.

In the low magnetic field regime however, we have to consider the new eigenstates $|+\rangle$ and $|-\rangle$ and the two-qubits states $|0, \pm\rangle$ and $|\mp, 0\rangle$. These terms are still not fully resonant because of the splitting between the $|+\rangle$ and $|-\rangle$ states caused by the local electric field, but they are close enough in energy that the double flip processes are not entirely quenched.

The computation of the depolarization rate including the double flips is detailed in appendix [REF]. To obtain a numerical value, we need to input the experimental values of the dipole-dipole interaction range [3] which we measured to be $\Gamma = 8.8$ MHz in Fig. [REF], as well as the average splitting $\Delta\nu$ between the $|+\rangle$ and $|-\rangle$ states. We typically measure $\Delta\nu \approx 8$ MHz on type Ib HPHT samples.

For the value presented in Fig. 1.1, we inputted $\Gamma = \Delta\nu = 8.8$ MHz.

1.2.4 T_2^* increase

The last aspect we considered was the change in the ODMR lineshape discussed in sec. 1.1.3 for weak magnetic field (we refer to the spectral linewidth as T_2^* for conciseness).

To quantify the impact of the T_2^* increase in the depolarization rate, we employ eq. [REF], where we use the values $2\gamma_f = 6.5$ MHz estimated in the last chapter and we take for $\Gamma_f = \Gamma_{NV}$ the values of half width at half maximum found in Fig. 1.2. We then find that the increase of T_2^* in zero magnetic field occasions an increase of the decay rate by $\sim 9\%$ for sample Sumi-2, and by $\sim 24\%$ for sample CVD-pink.

The value shown in Fig. 1.3 corresponds to a 9% increase.

In conclusion, we predict that the 4-classes degeneracy is by far the dominant causes for low field depolarization ($\sim \Gamma_1 \times 40$), followed by the double flips ($\sim \Gamma_1 \times 2$). We will however see in sec 1.5 that the double flips, along with the change of eigenbasis and increase in T_2^* are determinant factor in the sensitivity of the low field magnetometry protocol.

In the following section we will confront the theoretical results with experimental ones.

1.3   Experimental investigation of the low field depolarization

In this section we will try to experimentally discriminate the contribution of the four depolarization sources described in Fig. 1.3 and confront the experimental values with the theoretical ones.

---

[3]By interaction range we mean the value to be compared to the spectral detuning $\Delta\nu$ between the two groups. This is $2\gamma_f + \Gamma_{NV} + \Gamma_f$ in eq. [REF]

We will first determine the contribution of the 4-classes degeneracy by comparing [100] aligned and non-[100] aligned magnetic field in the weak magnetic field regime, before studying the influence of the double-flips thanks to purely transverse magnetic fields.

On top of the four previously discussed relaxation mechanisms, we have also considered two additional causes for the observation of low-field depolarization: the misalignment of the magnetic field (when $\mathbf{B} \parallel [100]$) and the influence of the laser polarization. Following further experiments detailed in appendix [REF], we have determined that these two effects were negligible compared to the four ones we identified before.

1.3.1 NV-NV CR in the low magnetic field regime

In this part, we will try to isolate the contribution of the 4-classes degeneracy from the three other ones by using the fact that all four classes can be at resonance for two distinct scenario:

- When $\mathbf{B} = 0$.

- When $\mathbf{B} \parallel [100]$ (cf. Fig. [REF] (la figure avec toutes les config)).

Magnetic scan in a random direction

First we will run a control experiment by scanning the magnetic field in a non [100] direction. Fig. 1.4-a) and b) shows ODMR spectrum at the starting point ($|\mathbf{B}| = 0$) and end point ($|\mathbf{B}| \approx 60$ G) of the magnetic field scan. The magnetic field orientation was chosen in order to maximize the splitting of the four classes.

Fig. 1.4-c) and d) show the evolution of the NV PL and stretched lifetime T_1^{dd}, defined in the last chapter [REF], as a function of the magnetic field. We can observe a decrease of T_1^{dd} by a factor of ~ 10 in zero magnetic field compared to non-zero magnetic field, with a half-width at half maximum of ~ 10 G. Correspondingly, we can observe a drop in PL by $\sim 4\%$ in zero magnetic field [4].

We attribute the spin depolarization observed in Fig. 1.4-d) to all four mechanisms described in the last part acting simultaneously. To determine the contribution of each mechanism individually, we will need to run dedicated experiments.

Magnetic scan with B $\parallel$ [100]

This second experiment is similar to the last one except that the magnetic field was scanned in the [100] direction. Fig. 1.5-a) and b) again show

---

[4]We can also note the decrease in PL for $|\mathbf{B}| > 30$ G is not corroborated by an increase of $1/T_1^{\mathrm{dd}}$. This is because this drop of PL is associated with transverse magnetic field state mixing, and not with spin depolarization.
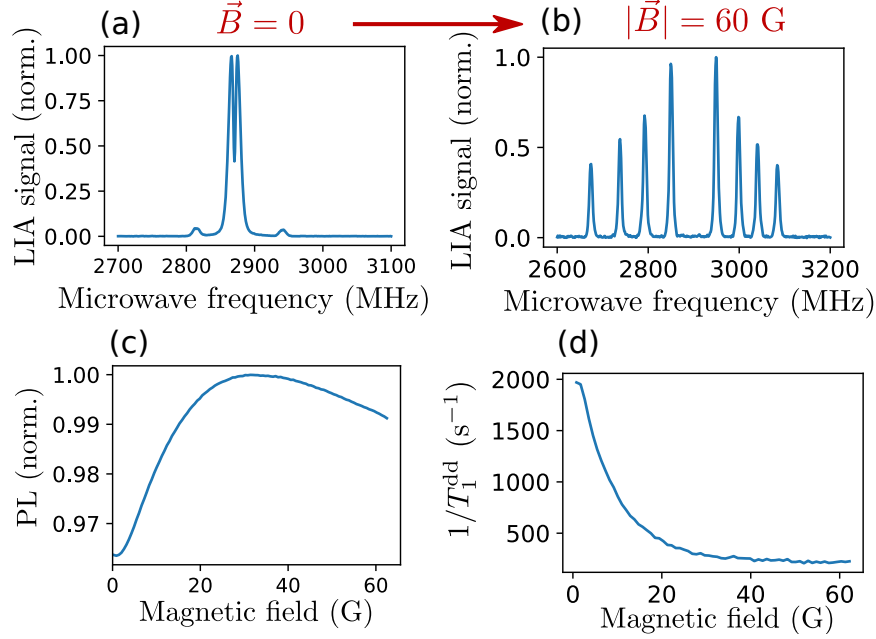
Figure 1.4: Low field depolarization on sample ADM-150-1 for **B** in an arbitrary direction. a) ODMR spectrum for B=0. b) ODMR spectrum for B=60 G. c) PL contrast as a function of the external magnetic field. d) $1/T_1^{\mathrm{dd}}$ as a function of the external magnetic field. A T_1 measurement was recorded for each magnetic field value and fitted accorded to the protocol described in [REF] with $T_1^{\mathrm{ph}} = 5$ ms

ODMR at the starting and ending point of the magnetic scan, while Fig. 1.5-c) and d) show the PL and $1/T_1^{\mathrm{dd}}$ recorded during the scan.

The main difference with the previous experiment is that in this case, the degeneracy between the four classes is never lifted. We therefore attribute the increase in $1/T_1^{\mathrm{dd}}$ at low magnetic field to the three other identified mechanisms. The increase in the depolarization rate in zero field (~ 20 %) as well as the decrease inPL ($\sim 0.5\%$) are still present, but significantly smaller than in the previous case. We can note however that the half-width at half maximum of the zero field depolarization (~ 2 G) is also smaller in this case.

We can also note a drop in PL and a corresponding increase of $1/T_1^{\mathrm{dd}}$ for $B \sim 20$ G which corresponds to the NV$-^{13}$C-NV cross-relaxation discussed in [REF]. We can not explain however why the depolarization rate appear to be smaller at $B \sim 10$ G than it is for $B > 30$ G.

The fact that the increase of the depolarization rate at zero field is about ~ 50 times weaker in Fig. 1.5 than it was in Fig. 1.4 confirms that the leading cause of depolarization in zero field is the degeneracy between the four classes of NV centers.
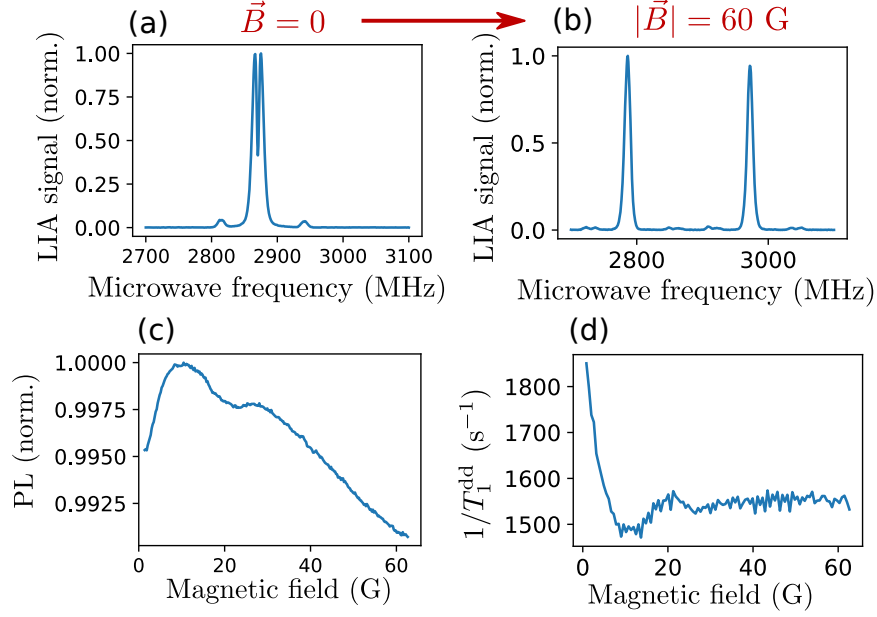
10

Figure 1.5: Same measurements as Fig. 1.4, still on sample ADM-150-1, but with **B** along the [100] axis.

1.3.2 NV-NV CR under purely transverse magnetic field

Thank to the two previous experiments, we were able to discriminate the contribution of the 4-classes degeneracy from the three other mechanisms that are which are the eigenbasis change, the double-flips and the T_2^* increase. We now seek to discriminate the contribution of each of these three mechanisms.

We unfortunately were not able to discriminate the change of eigenbasis from the T_2^* increase, which would likely require a statistical study over different samples with different T_2^* values. We were however able to discriminate the double flip contribution from the two other ones by scanning the magnetic field in a direction orthogonal to one NV class (**B** $\perp$ [111]).

Principle of the experiment

The idea behind the experiment is that the Hamiltonian eigenbasis is the same (or close to be the same) when **B** = 0 than it is when **B** $\perp$ [111], as described in sec. 1.1.2. For simplicity, we will assume here that both the magnetic field and the transverse electric field lies along the NV x axis : **B** = $B_x \hat{e}_x$ and **E**$_\perp$ = $E_x \hat{e}_x$

Fig. 1.6 shows a simulation of the eigenstates and eigenenergies for a NV Hamiltonian subject to transverse electric field and magnetic field. We labeled the eigenstates of the Hamiltonian $|1\rangle$, $|2\rangle$ and $|3\rangle$ in ascending order
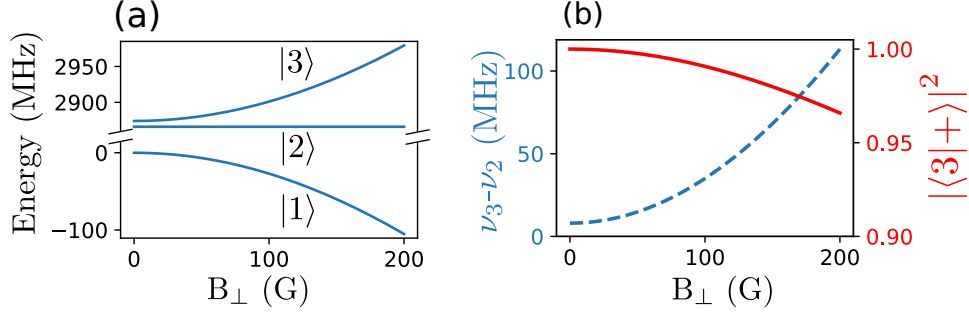
Figure 1.6: Simulation of the eigenstates of the NV Hamiltonian for a purely transverse magnetic field $B_\perp$. In addition to the transverse magnetic field, we consider a fixed transverse electric field of value $d_\perp E_\perp = 4$ MHz. (a) Eigenvalues for the spin Hamiltonian as a function of $B_\perp$. The three states are labeled $|1\rangle$, $|2\rangle$ and $|3\rangle$. (b) Splitting between the $|2\rangle$ and $|3\rangle$ states (blue curve) and closeness factor $|\langle 3|+\rangle|^2$ between the $|3\rangle$ and $|+\rangle$ (red curve)

of energy.

Fig. 1.6-b) shows both the splitting $\Delta\nu$ between the $|2\rangle$ and $|3\rangle$ states, and how close the $|3\rangle$ state is to the $|+\rangle = \frac{|+1\rangle+|-1\rangle}{\sqrt{2}}$ state via the factor $|\langle 3|+\rangle|^2$. We should note that with the assumption that $B_\perp \parallel E_\perp$, the $|2\rangle$ state is strictly equal to the $|-\rangle$ state regardless of the magnetic field amplitude.

These two metrics, $\Delta\nu$ and $|\langle 3|+\rangle|^2$ are what we are interested in for the experiment: we want to increase $\Delta\nu$ to the point where the double flips are completely quenched, but we want $|\langle 3|+\rangle|^2$ to remain close to 1 in order to preserve the eigenbasis and T_2^* contribution. Based on the plots in Fig.1.6-b), the region with $B_\perp \in [100 \text{ G}, 200 \text{ G}]$ seems to satisfy both these criteria: $\Delta\nu \,(100 \text{ G}) \approx 30$ MHz $\gg \gamma_f$[5] and $|\langle 3|+\rangle|^2 \,(200 \text{ G}) \approx 0.96$.

Ideally, we would have used an electric field instead of a transverse magnetic field to split the 4 classes energetically, but such an electric field would need to be $> 10^6$ V/cm which is several order of magnitudes greater than the breakdown voltage of air and out of our experimental reach.

Results

Fig. 1.7-a) shows an ODMR spectrum for $B = 20$ G with the two central lines corresponding to the $|0\rangle \to |+\rangle$ and $|0\rangle \to |-\rangle$ transitions of the class orthogonal to the magnetic field. We decided to start the scan of the magnetic field at 20 G because the class orthogonal to **B** was far enough ($> 20MHz$ MHz) from the three other ones that flip-flop between them

---

[5]Technically, we want to compare $\Delta\nu$ with the dipole-dipole interaction width $2\gamma_f + \Gamma_{NV} + \Gamma_f$ which we measured to be $\Gamma = 8.8$ MHz in Fig. [REF].
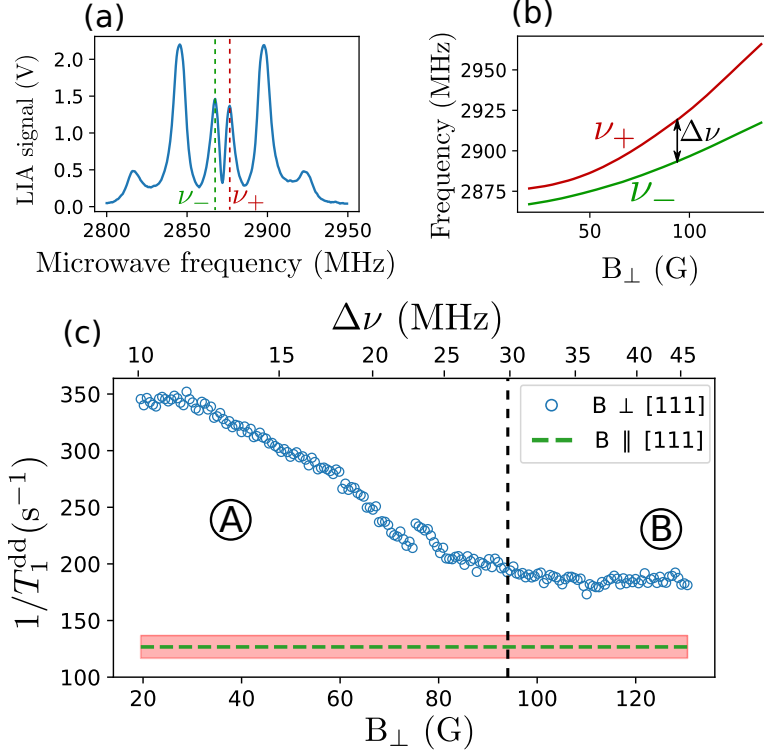
Figure 1.7: Experimental data for the depolarization under purely transverse magnetic field on sample ADM-150-2. a) ODMR spectrum for $|\mathbf{B}| = 20$ G. The transitions of the class orthogonal to the magnetic field are labeled ν_+ and ν_-. b) Dependency of ν_+ and ν_- with the magnetic field, as measured through ODMR. c) Measurement of T_1^{dd} as a function of the transverse magnetic field. The corresponding energy splittings $\Delta\nu = \nu_+ - \nu_-$ are written on top. We divided the plot between the A region where $1/T_1^{\mathrm{dd}}$ decreases, and the B region where it reaches a plateau with a value $1/T_1^{\mathrm{dd}} = 185 \pm 5$ s^{-1}. We also indicate in green the value found for a purely longitudinal magnetic field $1/T_1^{\mathrm{dd}} = 126 \pm 10$ s^{-1}

could be neglected[6]

Fig. 1.7-b) shows the evolution of the ν_+ and ν_- transition frequencies as a function of the magnetic field, measured via ODMR. The difference in frequency $\Delta\nu = \nu_+ - \nu_-$ is at first determined by the transverse electric field (~ 9 MHz) and then grows qudratically with the transverse magnetic field up to a value of ~ 50 MHz.

Fig. 1.7-c) shows the evolution of $1/T_1^{\mathrm{dd}}$ on a single class as a purely transverse magnetic field is scanned from 20 to 130 G. It also includes the

---

[6]The small plateau at the beginning of the $1/T_1^{\mathrm{dd}}$ curve in Fig. 1.7-c) confirms that flip-flop between the class orthogonal to $\mathbf{B}$ and the three other classes are indeed negligible compared to the other depolarization factors.

$1/T_1^{\mathrm{dd}}$ value found for a purely longitudinal magnetic field which we will consider as a baseline, since the eigenbasis in this case is $|\pm 1\rangle$ and not $|\pm\rangle$. We have divided the graph in two regions labeled A and B:

In region A, $1/T_1^{\mathrm{dd}}$ decreases with the magnetic field. The difference in the depolarizing rate between the $\mathbf{B} \perp [111]$ case and the $\mathbf{B} \parallel [111]$ case comes from the double flips, the eigenbasis change and the T_2^* increase. We measure an increase by a factor ~ 3 for B=20 G compared to the baseline.

In region B, $1/T_1^{\mathrm{dd}}$ reaches a plateau with a value of ~ 180 s^{-1}. We attribute this plateau to the fact that the double flips are completely quenched, which is coherent with the fact that $\Delta\nu \geq 30$ MHz. The remaining difference between the $\mathbf{B} \perp [111]$ and $\mathbf{B} \parallel [111]$ cases therefore comes from the eigenbasis change and the T_2^* increase. This increase amount for $\sim 50\%$ of the relaxation rate baseline.

We should note that the theoretical increase from the double flips and the change of eigenbasis[7] are not the values shown in Fig. 1.3: those were computed for a 4-class resonance, while we are looking here at a single class. The theoretical increase of the depolarization rate for a single class are detailed in Appendix [REF]. They are:

- $\Gamma_1^{|\pm\rangle} = 4\Gamma_0$ when taking into account the change of eigenbasis.

- $\Gamma_1^{dd} = [REF]\Gamma_1^{|\pm\rangle} = [REF]\Gamma_0$ when taking into account the double flips.

We have labeled here Γ_0 the relaxation rate coming from the flip-flop inside of a single class in the $|\pm 1\rangle$ basis (same definition as in table [REF] (table des valeurs chap 3). Experimentally, Γ_0 corresponds to the baseline shown in Fig. 1.7-c).

Although we find again that the fluctuator model overestimates the actual relaxation rates, these experimental observations still confirm the qualitative predictions of the model. In particular, they confirm that the double-flips are the second leading cause of zero-field depolarization after the 4-classes degeneracy.

1.3.3   Conclusion of the experimental observation

Fig. 1.8 summarizes the experimental results of this section. We explicitly indicates which of the four depolarization mechanisms are responsible for the observed depolarization rate at the beginning and at the end of each curve.

The experiments confirm the overall predictions of the previous section: the dominant cause of depolarization in zero magnetic field is the degeneracy of the 4 NV classes, followed by the double-flips and then by the eigenbasis change and T_2^* increase.

---

[7]The T_2^* increase should still amount for $\sim 10\%$.

(a) Random $\vec{B}$ direction

- 4-classes degeneracy
- Eigenbasis change
- Double-flips
- T_2^* change

- ~~4-classes degeneracy~~
- ~~Eigenbasis change~~
- ~~Double-flips~~
- ~~T_2^* change~~

(b) $\vec{B} \parallel [100]$

- 4-classes degeneracy
- Eigenbasis change
- Double-flips
- T_2^* change

- 4-classes degeneracy
- ~~Eigenbasis change~~
- ~~Double-flips~~
- ~~T_2^* change~~

(c) $\vec{B} \perp [111]$

- ~~4-classes degeneracy~~
- Eigenbasis change
- Double-flips
- T_2^* change

- ~~4-classes degeneracy~~
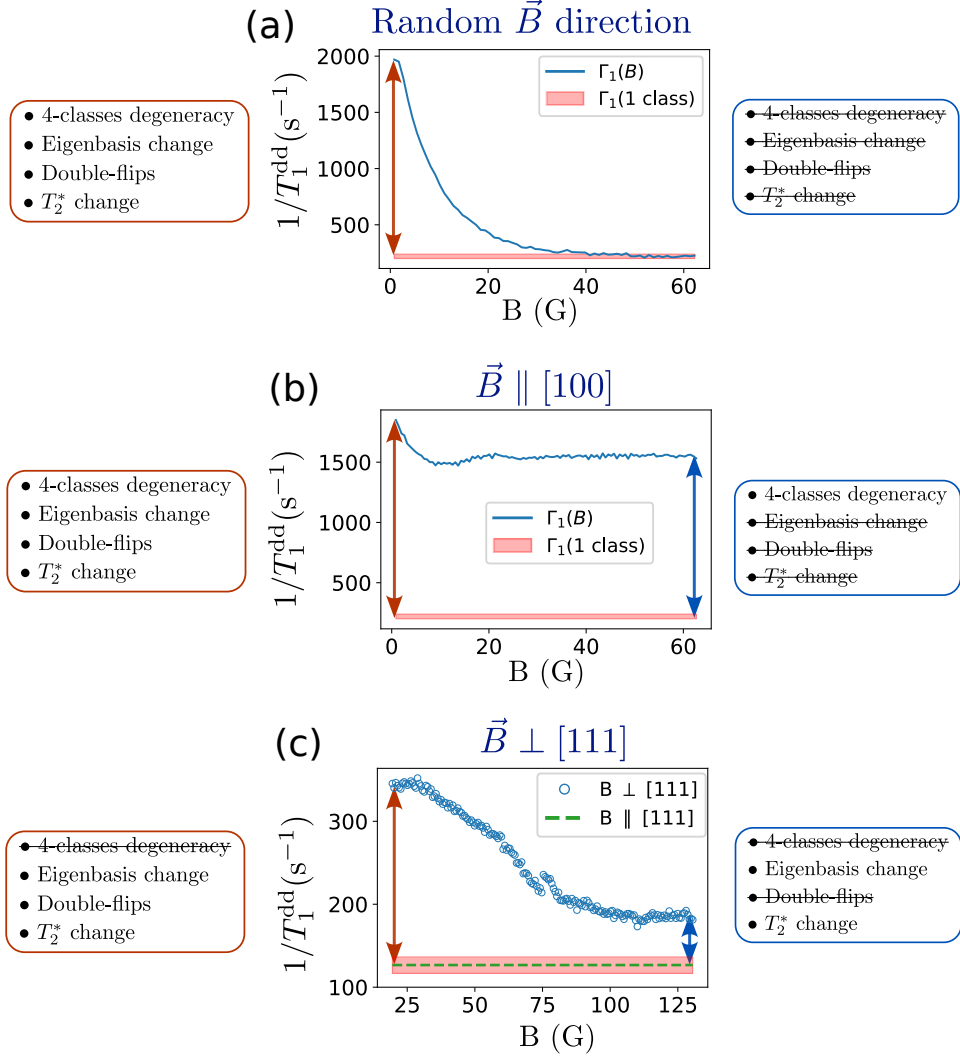- Eigenbasis change
- ~~Double-flips~~
- T_2^* change

Figure 1.8: Summary of the different experimental investigation. A baseline value is indicated with the pink shaded region in all experimental plots. The left box indicates the relaxation mechanisms added compared to the baseline for the minimum value of B, and the right box those for the maximum value of B. (a) corresponds to Fig. 1.4-d) where the baseline was measured to be 220 ± 20 s^{-1}, (b) corresponds to Fig. 1.5-d) with the same baseline, and (c) corresponds to Fig. 1.7-c).

We will now cover the low-field magnetometry protocol, after a quick overview of the field of NV magnetometry, and see the role that the different depolarization mechanisms play in it.

1.4 Introduction to ensemble NV magnetometry

There are two classes of NV magnetometer: single NV or ensemble. Single NVs offer a spatial resolution limited only by how far the magnetic source can be from the NV center (down to ~ 10 nm), but at the cost of a relatively low sensitivity (typically $\sim \mu\text{T}/\sqrt{\text{Hz}}$ [15]).

Ensemble NV centers center on the other hand offer sensitivities as low as 1 pT/$\sqrt{\text{Hz}}$ [16], at the cost of working with samples of sizes up to several mm.

We will only focus in this section on NV ensemble magnetometry since we want to give elements of comparisons with our technique based on NV-NV CR. We will not try to give a complete overview of this field, but only of the elements close to the technique we present. For a general overview on NV magnetometry, we recommend the excellent reviews [17–19].

1.4.1 AC and DC magnetometry

The most sensitive NV magnetometry protocols use the free precession of the spins to map a small change in the Zeeman energy into the phase of the spins, which is then converted into spin population. These protocols are generally separated between DC-broadband and AC-narrow band.

For DC-broadband magnetometry, the general technique consists of a Ramsey interferometry experiment, presented in chapter 1, the sensitivity of which is limited by the spin inhomogeneous coherence time T_2^* (which can reach up to μs for NV ensembles). The bandwidth of the protocol is limited by the repetition rate of the experiment, generally up to ~ 100 kHz. Although less sensitive in theory, continuous-wave (CW) ODMR and pulsed ODMR are also often employed for DC magnetometry. The state of the art DC ensemble magnetometr operates with a sensitivity of ~ 20 pT/$\sqrt{\text{Hz}}$ [20, 21].

For AC magnetometry, the basic protocol consists of a spin echo measurement, also presented in chapter 1, which extends the coherence time T_2^* to $T_2 = 10 \sim 100\mu s$, and which can be extended even further to $\sim$ ms times with dynamical decoupling [22]. Due to the longer "free" precession time, a larger phase can be imprinted on the spin for a similar magnetic field. The AC magnetic field however has to be in phase with the rephasing pulses, which limits the AC sensing to a relatively narrow band. The state of the art in term of AC sensing is ~ 1 pT/$\sqrt{\text{Hz}}$ [16].

Recently, [23] have achieved new records in both DC (~ 200 fT/$\sqrt{\text{Hz}}$) and AC (~ 10 fT/$\sqrt{\text{Hz}}$) NV magnetometry by using flux concentrators which are ferromagnets concentrating the magnetic field in a small volume, similarly to an electromagnet. The technology of flux concentrator could be applied to any NV magnetometry protocol. We will here only compare experimental results obtained without a flux concentrator.

1.4.2   Low field magnetometry

Magnetometry at low magnetic fields ($\gamma B < d_\perp E_\perp$) is challenging since in this regime the NV eigenstates and eigenenergies do not depend on the magnetic field to the first order. This complication is often lifted by simply using a bias magnetic field.

Some systems however need to be kept under low to zero external magnetic fields, for example to study the J-coupling between spins [24], or the phase of skyrmions [25]. To study these systems with NV centers, new protocols for low field NV magnetometry are required.

The main technique for low field magnetometry consists in using circularly polarized microwaves, which can only excite the $|0\rangle \rightarrow |-1\rangle$ and $|0\rangle \rightarrow |+1\rangle$ transitions, even when these states are not the Hamiltonian's eigenstates [26–29]. These states are linearly dependent on the magnetic field and can therefore be used to perform magnetometry. The best sensitivity achieved with this technique was 250 pT$/\sqrt{\text{Hz}}$ [27].

Another technique consists in using the ^{13}C$-$NV complex we discussed in sec. [REF] which because of the magnetic field offset caused by the ^{13}C nucleus are first order sensitive to the magnetic field even in zero external magnetic field [30]. With natural abundance ^{13}C however, this means that only $\sim 3\%$ of the NV centers are used, and increasing the ^{13}C concentration can lower the coherence of the NV centers.

1.4.3   Microwave-free DC magnetometry

All the previously described magnetemetry protocols relied on the use of a controllable microwave field to coherently manipulate the NV spin state.

The DC microwave-free protocols rely on sharp features in the PL for specific magnetic fields values. Fig. [REF] in chapter 2 show such PL features, in particular the ground state level anti-crossing (GSLAC, simply labeled LAC on the figure), the sharpest of these features.

The GSLAC occurs for a purely longitudinal magnetic field where $\gamma B_z = D$, which corresponds to $B = 1024$ G. In these conditions, the normally bright $|0\rangle$ state and the dark $|-1\rangle$ state become resonant and any residual mixing between these two states (coming from the electric field, the strain or the residual transverse magnetic field) will cause a drop in the NV polarization, and in the PL [31].

A protocol based on the GSLAC line has been implemented, first only for longitudinal magnetic field measurements [32] and then for 3D vector measurement [33] with a sensitivity ~ 300 pT$/\sqrt{\text{Hz}}$.

Another DC microwave-less protocol was proposed based on NV-NV CR [1, 2]. This technique reconstructs the external magnetic field by scanning an other magnetic field, similar to Fig. [REF] in chapter 3, and by measuring the position of the NV-NV CR lines. By scanning the magnetic field in

different directions, one can then recover the initial 3D magnetic field. The author of this paper did not measure the sensitivity of this protocol, but they predict a shot noise limited sensitivity of 24.7 nT/$\sqrt{\text{Hz}}$.

1.4.4 Orientation-free magnetometry

All protocols described so far require precise knowledge of the Larmor frequency between the $|0\rangle$ and $|\pm 1\rangle$ states for a given magnetic field. This knowledge implies that the direction of each NV axis in the frame of the magnetic field is known, because of the strong anisotropy in the NV Hamiltonian.

For a single crystal, these axes can always be calibrated through ODMR. However, for a polycrystalline diamond, diamond powder or even a single diamond with an erratic motion, the knowledge of these axes is not possible. New protocols need to be found if one wants to perform magnetometry with these materials.

To our knowledge, the only known orientation-free protocol for DC magnetometry is to use the change in PL caused by the transverse field, which is a property that depends only weakly on the field orientation, especially with an ensemble of NV centers with multiple axes. This protocol has an very low sensitivity and found limited use so far[**maletinsky2012robust**, 37–40].

Orientation-free magnetometry can also be performed for noise sensing, provided that that the noise is sufficiently broadband to directly excite the NV transitions regardless of their Larmor frequencies. The noise can be probed either by measuring the spin T_1 time [41, 42] (which does not require a knowledge of the Larmor frequency), or via the PL [43].

1.5 Low field depolarization magnetometry

We will now present and characterize the low field depolarization magnetometry (LFDM) protocol which rely on the depolarization of dense NV ensemble at low magnetic field. This protocol works for DC or slowly varying ($\lesssim 10$ kHz) magnetic field, is microwave-free, orientation-free, and operates at low magnetic field, although a small additional AC field is required to improve performances.

We will first describe its operation and characterize it before comparing it to the previously mentioned NV magnetometry protocols.

1.5.1 Principle of the experiment

Fig. 1.9 shows the principle of the LFDM protocol. The experimental setup is similar to the one presented in Fig. [REF] with the exception that there are no microwaves, and that the magnetic field generated by the
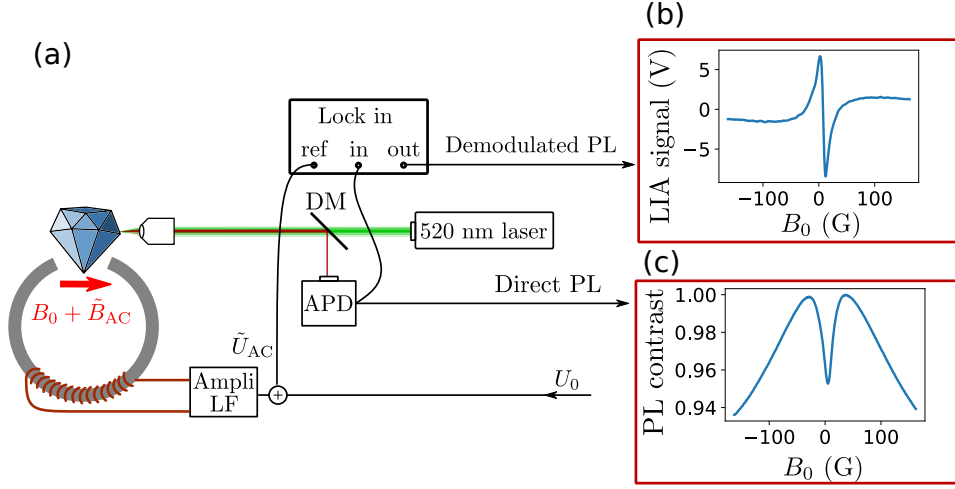
Figure 1.9: Principle of the LFDM protocol a) Experimental setup. The confocal microscopy setup is similar to the one described in [REF], the lock-in amplifier (LIA) is used here to add a modulation on the magnetic field, instead of the microwave. Both the PL and the LIA signal are monitored. b) example of LIA signal on sample ADM-15-4 when scanning the magnetic field B_0 between -150 and 150 G. c) PL signal corresponding to the LIA signal

electro-magnet contains both a DC or slowly variable component B_0 and an oscillating component $\tilde{B}_{AC}$ used for the modulation. We typically use a modulation frequency $f_{mod} \approx 1$ kHz, the same value we use for ODMR measurements. The main voltage V_0 responsible for the DC field and the oscillating voltage $\tilde{V}_{AC}$ responsible for the AC field are summed via a home-made bias tee.

Fig. 1.9-b) and c) show the PL measured on the photodiode and on the lock-in respectively, when the DC magnetic field is slowly varied ($f_{scan} <$ 1 Hz) from -150 to +150 G. For this configuration, the magnetic field was randomly oriented with respect to the NV axes and did not match any particular crystalline axis.

Both AC (up to ~ 10 kHz) and DC-magnetometry are possible with this setup. To improve the sensitivity however, an AC field needs to be added for the DC sensing, and inversely a DC field needs to be added for the AC sensing. Both of these added fields are typically of a few G for optimal performances, which limits the ultra-low field applications.

Fig. 1.10 shows how the AC and DC sensing work for LFDM: for DC sensing the LIA signal around $B_0 = 0$ provide a sharp linear slope to convert the LIA voltage into a magnetic field. For AC sensing, the LIA signal is directly proportional to the amplitude of the field. The optimal AC field amplitude for DC sensing has to match the width of the PL dip $|\tilde{B}_{AC}| =$
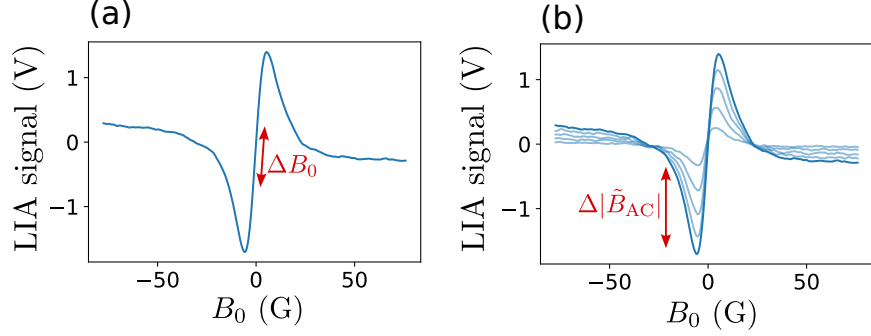
19

Figure 1.10: DC and AC LFDM sensing protocols on sample ADM-15-5. The magnetic field is scanned in an arbitrary direction. a) DC sensing: B_0 is scanned between -80 and $+80$ G while an AC field of amplitude 10 G is used for the lock-in detection. b) AC sensing: B_0 scans are performed for 5 different $|\tilde{B}_{AC}|$ values between 2 and 10 G. The best AC sensitivity is achieved for $B_0 \approx 5$ G.

$\sigma \approx 10$ G in order to maximize the slope of the lock-in signal around $B_0 = 0$. the optimal DC field to use for AC sensing is $B_0 = \sigma/2$ corresponding to the region where the lock-in signal is most sensitive to AC field.
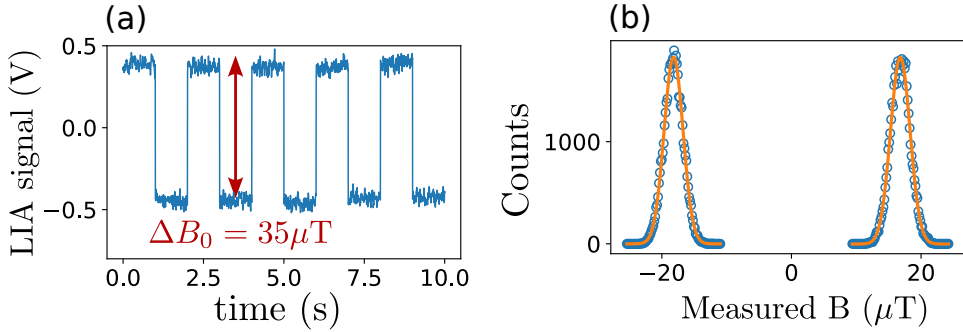
1.5.2 Sensitivity of the LFDM protocol

Figure 1.11: Sensitivity measurement of the LFDM on sample ADM-15-4. a) Temporal trace of the LIA signal when applying an alternating external magnetic field of amplitude 35 μT and frequency $f = 1$ Hz. b) Histogram of the DC measurement over 50 s. The data is fitted with Gaussians of width 1.6 μT.

We will now look at the performances of the LFDM protocol before comparing it to the other magnetometry protocols. The characterization was only done for DC sensing. The samples used for the characterization were 15 μm micro-diamond bought as is from Adamas nanodiamond (see

the sample section [REF] for more information).

We characterize the DC sensitivity by looking at the noise floor on the LIA signal when sitting on the steepest sloped ($B_0 \approx 0$). The following parameters were used: $|\tilde{B}_{AC}| \approx 10$ G and $f_{mod} \approx 1$ kHz, the laser power was ≈ 1 mW and the collected PL power ≈ 1 μW. The lock-in low-pass filter time constant was set to $\tau = 3$ ms.

Fig. 1.11 shows the sensitivity measurement protocol. First, the applied magnetic field is calibrated with ODMR spectra, then an alternating DC field of known amplitude (here $\Delta B_0 = 35$ μT) is applied on the sample. Fig. 1.11-a) shows the temporal trace of the LIA signal in response to this alternating DC field. Knowing the amplitude of the alternating field, we can then convert the voltage signal into a magnetic field amplitude, with in this case a ratio 45 ± 3 μT/V.

Fig. 1.11-b) shows an histogram of the measured magnetic field amplitude for both the high and low value of the applied magnetic field. The total acquisition time was 50 s with the external field being alternated every second. The histograms are nicely fitted with Gaussian profiles of width $\sigma = 1.5 \pm 0.1$ μT which allows us to estimate the DC sensitivity of the protocol:

$$\eta = \frac{\sigma}{\sqrt{2\tau}} = 116 \pm 10 \text{ nT}/\sqrt{\text{Hz}}, \qquad (1.9)$$

where $\tau = 3$ ms is the LIA low-pass filter time constant.

We estimate that the sensitivity is mostly shot-noise limited because the same LIA voltage noise ($\sqrt{\langle \delta V^2 \rangle} \approx 35$ mV) was observed on a magnetic insensitive region (for $B_0 \approx 100$ G), and is far above the electrical noise measured when no optical signal is sent to the photodiode ($\delta V < 1$ mV). Laser fluctuations could also play a role but the noise seem to grow as the square root of the optical power and not linearly with it.

1.5.3 Angular dependence of the sensitivity

We will now look at the dependence of the sensitivity with respect to the magnetic field angle. In particular, we are interested in comparing the sensitivity when $\mathbf{B} \parallel [100]$, where there is no lift of degeneracy between the four classes as $\mathbf{B}$ increases; and a case where $\mathbf{B} \nparallel [100]$ and where there is a lift of degeneracy between the four classes. We previously saw in Fig. 1.4 and 1.5 that the PL and T_1 contrast was much smaller when $\mathbf{B} \parallel [100]$, but we now focus on the sensitivity which is related to the slope of the PL change, and not directly to the contrast.

Fig. 1.12-a) and b) show the LIA signal when the DC field B_0 is scanned from -150 G to $+150$ G on the same sample ADM-15-4, but for two different angle of B_0. For the blue curve, the field was scanned along the [100] axis, for the orange curve, it was scanned with an angle of ~ 20 ° compared to the [100] axis. We can see that the maximum amplitude of the lock-in signal
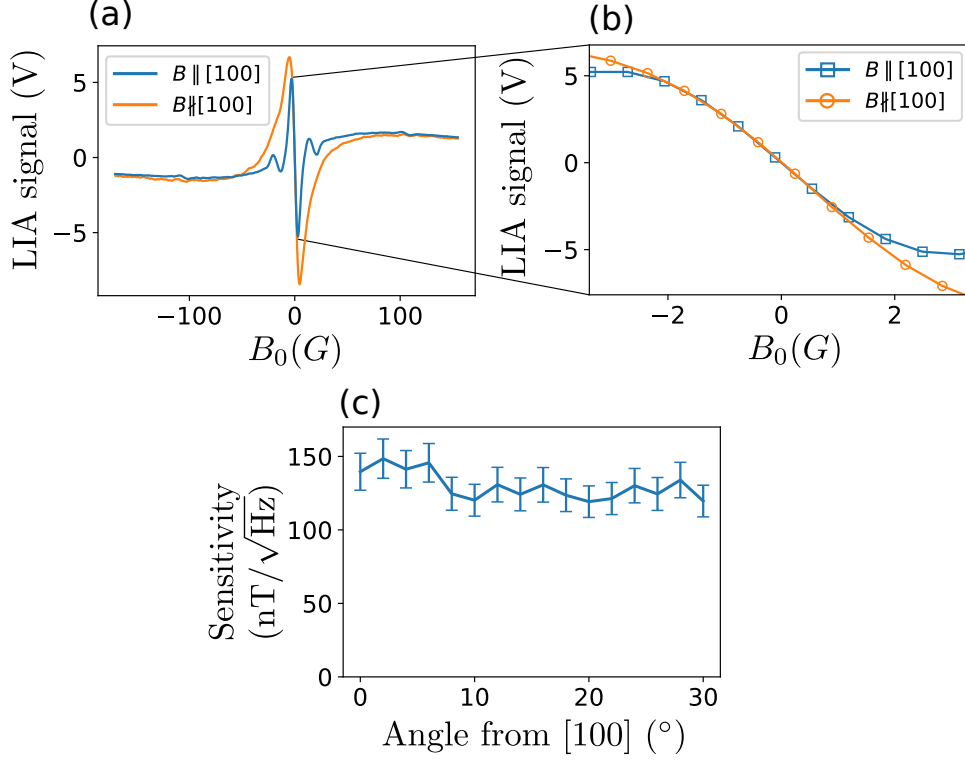
Figure 1.12: Angular dependence of the sensitivity. a) LIA signal for B_0 scanned between -150 and $+150$ G along the [100] axis, or along a direction 20° off the [100] axis. b) Zoom-in of the LIA signal on the zero-field slopes. c) Measured sensitivity as a function of the magnetic field angle with the [100] axis.

(relevant for AC sensing) is of the same order of magnitude for both case, and the slope around B_0 (relevant for DC sensing) is almost identical. Fig. 1.12-c) shows the sensitivity, measured with the protocol described in Fig. 1.11, with respect to the angle between the magnetic field and the [100] axis. We can notice that the sensitivity depends only weakly on the magnetic field angle.

The fact that the sensitivity is similar when **B** $\parallel$ [100] or **B** $\nparallel$ [100] means that the inter-class co-resonances plays a lower role in the sensitivity than the zero-field specific depolarization mechanisms, previously detailed in Sec. 1.2. We cannot be sure which of the three zero-field mechanism is the dominant one, but based on the experimental results shown in Fig. 1.7, we can assume that the double-flips are the dominant factor in the LFDM sensitivity.

It should be noted that this low angular dependence was particularly marked on sample ADM-15-4. Other samples, including from the same

batch, showed a higher angular dependence with typically a sensitivity $2 \sim 3$ times worse for $B \parallel [100]$ than for the other directions.
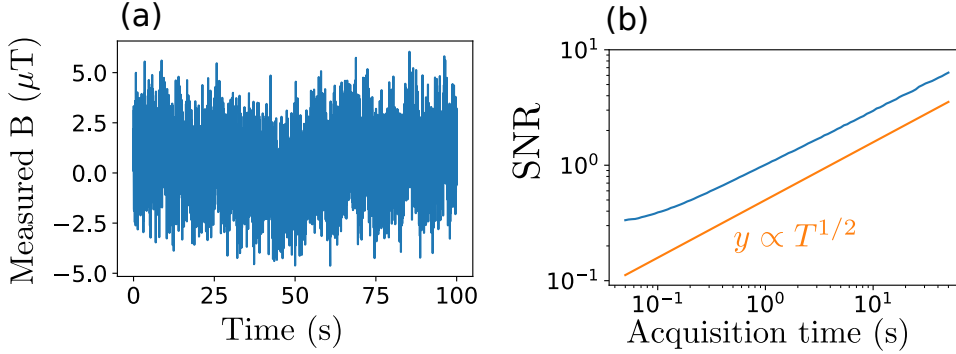
1.5.4   Temporal stability

Figure 1.13: Temporal stability of DC-LFDM as measured on sample ADM-15-5. a) Temporal trace of the LIA signal for $B_0 \approx 0$. The Lock-in signal was converted to a measured magnetic field with the previously described protocol. b) Estimated signal to noise ratio for a signal of 100 nT as a function of the total acquisition time T. The noise value is computed by averaging the variance of the temporal trace over each time duration T. A curve $y = 0.5\,T^{1/2}$ is added for comparison

An important aspect of sensors is their stability in time. The sensitivity being expressed in $\mathrm{nT}/\sqrt{\mathrm{Hz}}$ suggests that the signal to noise ratio (SNR) given by repeating the measurement increases as $\sqrt{T}$ where T is the total acquisition time. This is true for an ideal system, but in practice drifts and low frequency noise mean that the actual SNR for long acquisition time will be worse than the SNR at short time scaled by a factor $\sqrt{T}$.

One of the main source of drift for NV magnetometry based on spin resonance is the crystal lattice temperature change: the D factor in the NV Hamiltonian (eq. [REF]) is sensitive to the lattice temperature because of the thermal dilatation of the crystal, which is the basis for NV thermometry [44]. This means that thermal fluctuations will impact the Larmor frequency of the spins and may cause a detuning with the initial measured frequency for long acquisition times. The LFDM protocol however does not rely on a specific resonance frequency, but rather on a co-resonnance condition between neighboring spins, which does not depend directly on the crystal temperature.

Fig. 1.13 shows the temporal stability of the LFDM protocol over an acquisition time of 100 s. Fig. 1.13-a) shows a temporal trace of the LIA signal where we have converted the signal into a measured magnetic field. Fig. 1.13-b) shows the estimated SNR for a signal of 100 nT as a function

of the total acquisition time and was computed from the temporal trace.

We can see that the SNR does not deviate from the $\sqrt{T}$ scaling for times up to 50 s, and could probably be extended for longer times. The non-linearity for shorter times comes from the LIA low-pass filter.

1.6 Comparison between LFDM and other magnetometry protocol

Now that we have characterized the LFDM protocol, we can compare its performances with the previously mentioned magnetometry protocols. We should start by mentioning that the best sensitivity achieved with the LFDM ($\sim 100\mathrm{nT}/\sqrt{\mathrm{Hz}}$) is about 10^5 times worse than the best NV ensemble sensitivity. This discrepancy however come in large part to the smaller sensor volume used in the characterization, and to a relatively low PL collection efficiency compared to the other experiments.

1.6.1 Comparison with microwave based protocols

Table 1.1: Comparison of the volume-normalized sensitivity of the best AC and DC protocols with LFDM

	Zhou et al. [45] (AC)	Barry et al.[20] (DC)	LFDM (DC)
η (nT/$\sqrt{\mathrm{Hz}}$)	92	0.015	116
V (μm^3)	$8.1 \cdot 10^{-3}$	$5.2 \cdot 10^{6}$	$3.3 \cdot 10^{3}$
η_v (nTμm$^{3/2}$Hz$^{-1/2}$)	8.3	34	6700

We will first compare the LFDM protocol with the best microwave-based NV magnetometry protocols. A better metric than the sensitivity to compare different protocols is the volume-normalized sensitivity defined in [45] as $\eta_v = \eta \cdot \sqrt{V}$ where η is the sensitivity and V the effective volume of the sensor. This scaling assumes that each NV center in an ensemble is an independent magnetic field probe, and as the total number of NV centers is proportional to V, the sensitivity should scale as $1/\sqrt{V}$.

Table 1.1 reports the best AC and DC volume-normalized sensitivities found in the literature. The LFDM protocol performs ~ 200 times worse than the best DC magnetometer. It should be noted however that the PL collection in our measurement, where we use a confocal microscope with a numerical aperture NA=0.65, is estimated to be $\sim 1\%$ [46], while the best collection schemes [16, 35, 36, 46] achieve a collection efficiency above 50 %.

Fig. 1.14 shows a comparison between LFDM and microwave-based magnetometry using our setup. A fixed microwave tone (here at 2600 MHz)
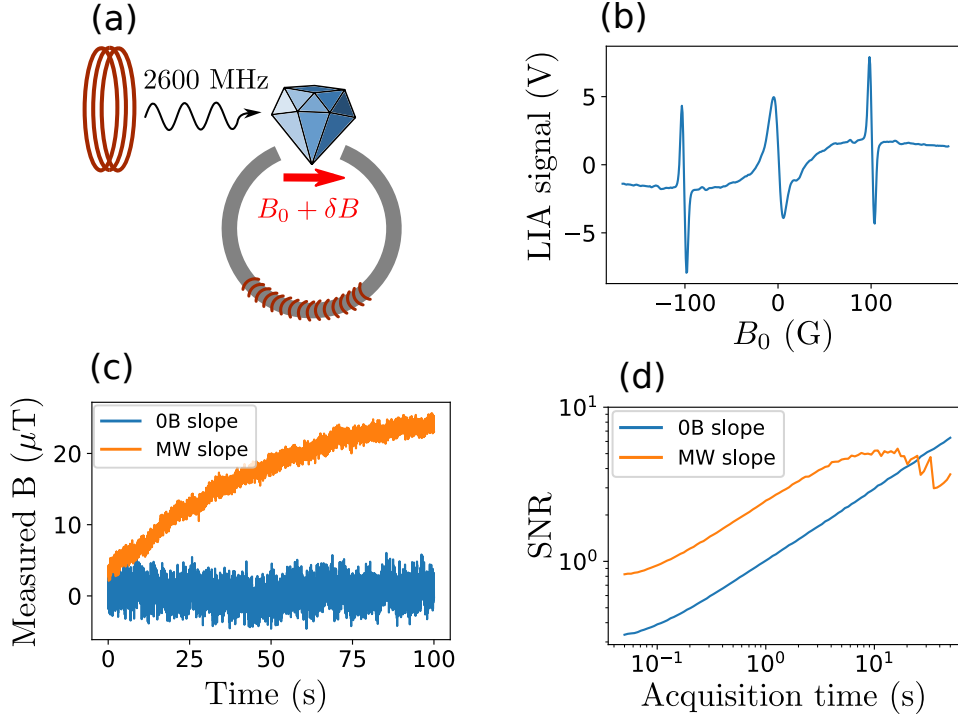
Figure 1.14: Comparison between LFDM and microwave-based magnetometry on the same experimental setup. The sample used is ADM-15-5 and the magnetic field is aligned close to a [111] axis. a) Schematics of the experiment: the setup is the same as the one described in Fig. 1.9 with the addition of a continuous microwave tone at the frequency $\nu = 2600$ MHz. b) LIA signal as B_0 is scanned from -150 to $+150$ G. The two lines at ± 100 G are caused by the microwave. c) Temporal trace of the measured B field for $B_0 \approx 0$ (on the middle of the zero field slope) and $B_0 \approx 100$ G (on the middle of the microwave slope). The orange curve is shifted by ≈ 100 G to sit on the same scale as the blue curve. d) Estimated SNR fo a signal of 100 nT for $B_0 \approx 0$ and $B_0 \approx 100$ G as a function of the total acquisition time

is sent to the diamond and a magnetic field B_0 close to the [111] axis is scanned along an oscillating field δB to perform a lock-in detection.

Fig. 1.14-b) shows the LIA signal over a B_0 scan: the profile is similar to the one in Fig. 1.9-b) with the addition to two sharp lines for $|B_0| \approx 100$ G. These two lines correspond to the transition $|0\rangle \rightarrow |-1\rangle$ (or $|0\rangle \rightarrow |+1\rangle$ for the negative fields) of the class aligned with the magnetic field when it comes to resonance with the 2600 MHz microwave tone. The microwave power used here correspond to a Rabi frequency $\Omega \approx (2\pi)3$ MHz and the slope on the steepest part of the microwave line is ~ 2.5 times higher than the slope in zero field.

Fig. 1.14-c) and d) show the temporal stability of the sensor similarly to

Fig. 1.13, on both the zero field line and the microwave line. While we can see that the microwave signal is more sensitive thanks to the higher slope, it is also more prone to drift, most likely because of the shift of the Larmor frequency caused by temperature fluctuations. We can even see that the LFDM becomes more sensitive for acquisition times beyond 10 s.

We should acknowledge that this microwave-based detection is not optimal: we are using a technique analogous to CW ODMR which is not as sensitive as Ramsey interference (although CW ODMR was also the technique used in [20]), we were limited in the available microwave power (although in this case $\Omega_{\mathrm{Rabi}} \sim 1/T_2^*$ which is supposed to be optimal), and the sample used here had a relatively poor $T_2^* \approx 68$ ns. Nevertheless, this shows that the LFDM protocol is not that far from basic microwave-based magnetometry with the samples and the optical setup used here.

1.6.2 Comparison with microwave-less protocols

The only microwave-less protocols to have measured a sensitivity are the GSLAC protocols described previously [32, 33]. Unfortunately the sensing volume in this studies is not known, however due to the similarity in our approaches, we should be able to directly compare the physical origin of both protocols, i.e. comparing the zero field PL dip and the GSLAC PL dip.

In Fig. 1.9-c) we can observe a PL dip with a contrast $C = 4.7 \pm 1\%$ for a full width at half maximum $\Gamma = 20 \pm 1$ G. In comparison, in [32] the authors observe a GSLAC PL dip with a contrast $C = 4.5\%$ for a full width of 12 G with a type Ib irradiated diamond, similar to the ones we use. In [33] they manage to keep a contrast of 4.5 % while reducing the GSLAC linewidth to 0.38 G by using a CVD sample isotopically enriched in ^{12}C with a lower [NV] and [N] density.

The zero field technique is therefore comparable with the GSLAC technique for samples with high NV and impurity concentration, but unlike the GSLAC magnetometry, it is still unclear what kind of material engineering would improve its sensitivity.

1.7 Conclusion and perspectives

We have seen in this chapter that dense ensemble of NV centers spontaneously depolarize at low magnetic field, and wee have seen that the depolarization is mediated by dipole-dipole coupling between the NV centers. We have identified three mechanisms by which the depolarization is increased in zero-field: the inter-class flip-flops, the double flips, and the change in the NV eigenstates (which includes the change in T_2^*).We have then quantified both theoretically and experimentally the contribution of each of these mechanisms to the zero-field depolarization.

Finally, we have seen how this low-field depolarization can be applied to perform magnetometry experiments, and what advantages and disadvantages this technique offers compared to the established NV magnetometry protocols.

We will now describe what could be interesting investigation points to further improve the LFDM performance, as well as potential applications.
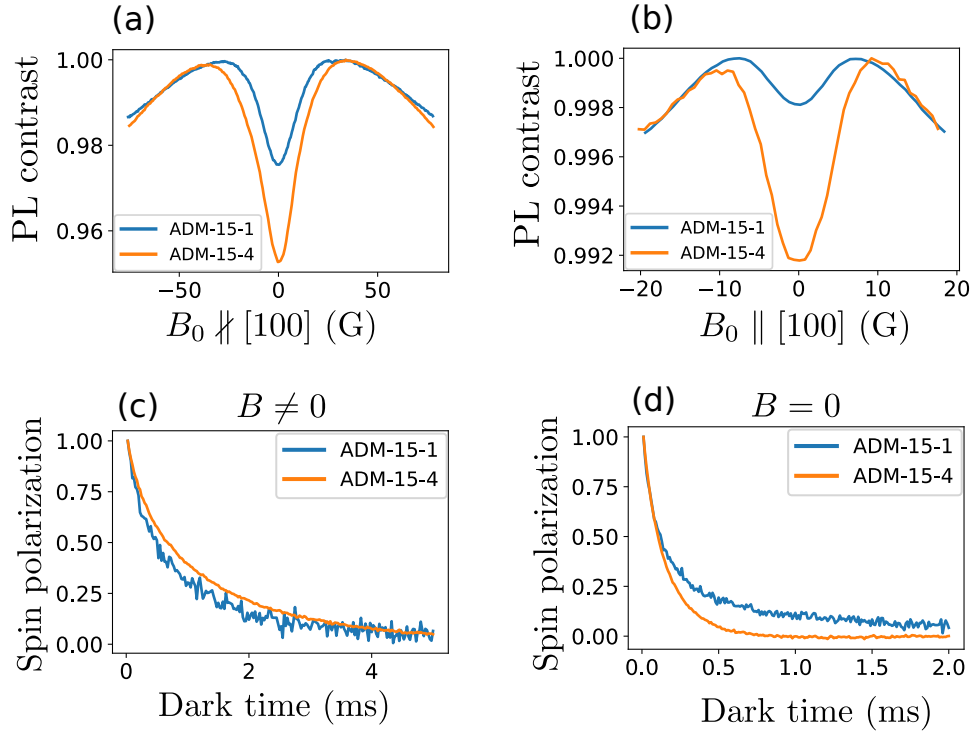
1.7.1 LFDM optimization

Figure 1.15: a) PL of two distinct samples ADM-15-1 and ADM-15-4 as the magnetic field is scanned in an arbitrary direction (which splits the 4 classes similarly in both cases). b) Same measurement with $B \parallel [100]$ c) T_1 measurement on both samples on a single class for $B \approx 50$ G. d) T_1 measurement on both samples on all four classes for $B = 0$.

Given the few parameters involved in the LFDM protocol, the main path for LFDM optimization seem to be the material optimization of the samples.

Most magnetometry protocols have a relatively clear material optimization path: DC protocols use the figure of merit ρT_2^* and AC protocols ρT_2, where $\rho = [NV]$ is the NV concentration. The reason is that the number of NV centers for a given volume scales as ρ, and therefore the sensitivity scale as $1/\sqrt{\rho}$. Meanwhile increasing the density of defects tend to decrease the spin coherence times T_2 and T_2^*, and the AC and DC sensitivities scale

respectively as $1/\sqrt{T_2}$ and $1/\sqrt{T_2^*}$. The sensitivity in both of these cases is then inversely proportional to the figure of merit.

For the LFDM protocol however, the material optimization is far from obvious. Indeed, while increasing T_2^* would improve the sensitivity, the gain might not be as interesting as for traditional protocols due to the broadening caused by γ_f. On the other hand, increasing the NV density not only increases the number of sensor per volume, but also increases the dipole-dipole strength between NV centers. If we assume that fluctuators are constituted of closely packed impurities, then increasing the NV density should also increase the fluctuator proportion.

Increasing the NV density seem to be the path for further material optimization, but other issues may arise in the process.

We should note that we observed large discrepancy in the zero field depolarization among the samples that we studied, even from samples coming from the same batch.

Fig. 1.15-a) shows the PL on two distinct 15-μm Adamas microdiamonds for a magnetic field scanned in a random direction, and Fig. 1.15-b) for a magnetic field scanned along the [100]. We can notice that the PL contrast in zero field is twice as big for sample ADM-15-4 when $B \nparallel [100]$, and 5 time as big when $B \parallel [100]$, which would directly impact their respective sensitivity in LFDM.

Fig. 1.15-c) and d) shows T_1 measurement on both samples either on a single class for $B \neq 0$ or for all four classes for $B = 0$. Interestingly, we can notice that the T_1 of sample ADM-15-1 is both shorter than the one of ADM-15-4 for $B \neq 0$, and longer for $B = 0$. This could indicate that another relaxation mechanism is competing with the NV-fluctuator one on sample ADM-15-1, which would limit the LFDM sensitivity.

Other non-material parameters in the LFDM protocols should also be investigated. This includes the temperature of the sample, the intensity and wavelength of the laser, the frequency and amplitude of the AC magnetic field.

1.7.2 Potential applications for LFDM

We will now turn to potential applications for LFDM, which could be useful even without material optimization.

Fig. 1.16 illustrates two potential applications for LFDM. The first one is to to perform wide-field magnetic imaging on a surface with micron-sized irregularities. The current leading technology for wide field imaging is to use a bulk CVD diamond with a very well polished surface in direct contact with the probed sample [47, 48]. While the diamond surface can be controlled within a few nm, the same is not always true for the sample, especially for paleomagnetism or biomagnetism samples. Furthermore, controlling the angle between the diamond and the sample can be challenging even for two
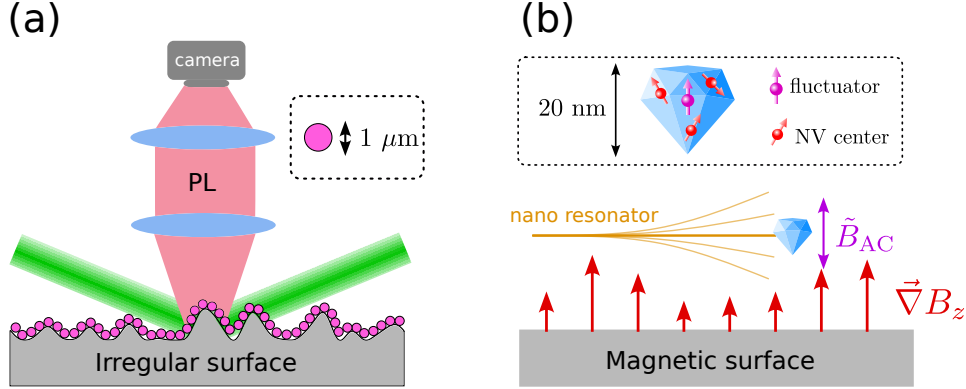
Figure 1.16: Schematics of two potential application for LFDM. The working of each application is detailed in the main text

perfectly flat surface.

Instead we propose to deposit a thin layer of 1 μm diamonds on top of the sample in order to always always have a sensor within ~ 1 μm of the sample. Going below 1 μm may not prove useful as the spatial resolution is ultimately limited by the diffraction limit of the lens. One advantage of this method is that commercially available samples (Adamas Nano 1 μm red fluorescent diamond) are well suited for this task. I have measured the sensitivity on some of these samples and found the same volumetric sensitivity $\eta_v \sim 6$ μTμm$^{3/2}$Hz$^{-1/2}$ than for the 15 μm samples. This sensitivity is already better than some previous applications of wide field imaging at 20 μTμmHz$^{-1/2}$ [49]. Another potential advantage of LFDM is that a homogeneous magnetic field or microwave intensity along the sample is not required. Only a ~ 10 G AC magnetic field is required, and the sensitivity does not depend critically on the AC field homogeneity.

Another potential application for LFDM is shown in Fig. 1.16-b. It consists in the detection of magnetic field gradient thanks to a nano-diamond probe attached to a nano-resonator. The resonator motion transform the DC gradient in an AC field which can then be probed following the protocol described in Fig. 1.10-b). This idea is based on previous work with NV centers [50] and magnetic resonance force microscopy (MRFM) [51]. A very similar protocol was recently developed with microwave based AC sensing [52].

In order to use AC LFDM with a scanning probe setup, one would need to have a nano-diamond with at least one NV center and one fluctuator. This may not be such a rare event: a $(20$ nm$)^3$ nanodimaond with [NV]=5 ppm contains on average ≈ 4 NV centers. If we take a fluctuator proportion of 30 % as measured in [53], then finding a nanodiamond with at least one NV and one fluctuator seems feasible. I have not studied the regime with few or single NV and fluctuator, which is in itself an interesting prospect,

and I therefore cannot estimate the sensitivity of such a probe.

Other potential applications for LFDM includes the possibility to use polycrystalline diamond, potentially grown through heteroepitaxy on top of a surface of interest, or to follow individual diamonds flowing in liquid or living organism, similar to what was done in [54], but without having to constantly calibrate the diamond axes through ODMR which significantly hinders the temporal resolution of microwave-based technique.

Finally, LFDM could be a good candidate to be scaled up since the protocol is not sensitive to strain or thermal variations and does not require a homogeneous magnetic field or microwave field along the sample.

Bibliography

[1] Rinat Akhmedzhanov et al. "Microwave-free magnetometry based on cross-relaxation resonances in diamond nitrogen-vacancy centers". In: *Physical Review A* 96.1 (2017), p. 013806.

[2] Rinat Akhmedzhanov et al. "Magnetometry by cross-relaxation-resonance detection in ensembles of nitrogen-vacancy centers". In: *Physical Review A* 100.4 (2019), p. 043844.

[3] C Pellet-Mary et al. "Spin-Relaxation of Dipolar-Coupled Nitrogen-Vacancy Centers: The role of Double-flip Processes". In: *arXiv preprint arXiv:2207.13899* (2022).

[4] MW Doherty et al. "Theory of the ground-state spin of the NV- center in diamond". In: *Physical Review B* 85.20 (2012), p. 205203.

[5] Péter Udvarhelyi et al. "Spin-strain interaction in nitrogen-vacancy centers in diamond". In: *Physical Review B* 98.7 (2018), p. 075201.

[6] Thomas Mittiga et al. "Imaging the local charge environment of nitrogen-vacancy centers in diamond". In: *Physical review letters* 121.24 (2018), p. 246402.

[7] Eric Van Oort and Max Glasbeek. "Electric-field-induced modulation of spin echoes of NV centers in diamond". In: *Chemical Physics Letters* 168.6 (1990), pp. 529–532.

[8] Michael SJ Barson et al. "Nanomechanical sensing using spins in diamond". In: *Nano letters* 17.3 (2017), pp. 1496–1503.

[9] Ziwei Qiu et al. "Nuclear spin assisted magnetic field angle sensing". In: *npj Quantum Information* 7.1 (2021), pp. 1–7.

[10] Ziwei Qiu et al. "Nanoscale Electric Field Imaging with an Ambient Scanning Quantum Sensor Microscope". In: *arXiv preprint arXiv:2205.03952* (2022).

[11] P Jamonneau et al. "Competition between electric field and magnetic field noise in the decoherence of a single spin in diamond". In: *Physical Review B* 93.2 (2016), p. 024305.

[12] Benjamin Smeltzer, Jean McIntyre, and Lilian Childress. "Robust control of individual nuclear spins in diamond". In: *Physical Review A* 80.5 (2009), p. 050302.

[13] SV Anishchik et al. "Low-field feature in the magnetic spectra of NV- centers in diamond". In: *New Journal of Physics* 17.2 (2015), p. 023040.

[14] DS Filimonenko et al. "Weak magnetic field effects on the photoluminescence of an ensemble of NV centers in diamond: experiment and modelling". In: *Semiconductors* 54.12 (2020), pp. 1730–1733.

[15] Matthew Pelliccione et al. "Scanned probe imaging of nanoscale magnetism at cryogenic temperatures with a single-spin quantum sensor". In: *Nature nanotechnology* 11.8 (2016), pp. 700–705.

[16] Thomas Wolf et al. "Subpicotesla diamond magnetometry". In: *Physical Review X* 5.4 (2015), p. 041001.

[17] LoïHERE!HERE!c Rondin et al. "Magnetometry with nitrogen-vacancy defects in diamond". In: *Reports on progress in physics* 77.5 (2014), p. 056503.

[18] Christian L Degen, Friedemann Reinhard, and Paola Cappellaro. "Quantum sensing". In: *Reviews of modern physics* 89.3 (2017), p. 035002.

[19] John F Barry et al. "Sensitivity optimization for NV-diamond magnetometry". In: *Reviews of Modern Physics* 92.1 (2020), p. 015004.

[20] John F Barry et al. "Optical magnetic detection of single-neuron action potentials using quantum defects in diamond". In: *Proceedings of the National Academy of Sciences* 113.49 (2016), pp. 14133–14138.

[21] Georgios Chatzidrosos et al. "Miniature cavity-enhanced diamond magnetometer". In: *Physical Review Applied* 8.4 (2017), p. 044019.

[22] Linh My Pham et al. "Enhanced solid-state multispin metrology using dynamical decoupling". In: *Physical Review B* 86.4 (2012), p. 045214.

[23] Yijin Xie et al. "A hybrid magnetometer towards femtotesla sensitivity under ambient conditions". In: *Science Bulletin* 66.2 (2021), pp. 127–132.

[24] Kiplangat Sutter and Jochen Autschbach. "Computational study and molecular orbital analysis of NMR shielding, spin–spin coupling, and electric field gradients of azido platinum complexes". In: *Journal of the American Chemical Society* 134.32 (2012), pp. 13374–13385.

[25] Jakub Zázvorka et al. "Skyrmion lattice phases in thin film multilayer". In: *Advanced Functional Materials* 30.46 (2020), p. 2004037.

[26] Mariusz Mrózek et al. "Circularly polarized microwaves for magnetic resonance study in the GHz range: Application to nitrogen-vacancy in diamonds". In: *Applied Physics Letters* 107.1 (2015), p. 013505.

[27] Huijie Zheng et al. "Zero-field magnetometry based on nitrogen-vacancy ensembles in diamond". In: *Physical Review Applied* 11.6 (2019), p. 064068.

[28] Till Lenz et al. "Magnetic sensing at zero field with a single nitrogen-vacancy center". In: *Quantum Science and Technology* 6.3 (2021), p. 034006.

[29] Philipp J Vetter et al. "Zero-and Low-Field Sensing with Nitrogen-Vacancy Centers". In: *Physical Review Applied* 17.4 (2022), p. 044028.

[30] Ning Wang et al. "Zero-field magnetometry using hyperfine-biased nitrogen-vacancy centers near diamond surfaces". In: *Physical Review Research* 4.1 (2022), p. 013098.

[31] David A Broadway et al. "Anticrossing spin dynamics of diamond nitrogen-vacancy centers and all-optical low-frequency magnetometry". In: *Physical Review Applied* 6.6 (2016), p. 064001.

[32] Arne Wickenbrock et al. "Microwave-free magnetometry with nitrogen-vacancy centers in diamond". In: *Applied Physics Letters* 109.5 (2016), p. 053505.

[33] Huijie Zheng et al. "Microwave-free vector magnetometry with nitrogen-vacancy centers along a single axis in diamond". In: *Physical Review Applied* 13.4 (2020), p. 044023.

[34] Simone Magaletti et al. "Quantum Diamond Radio Frequency Signal Analyser based on Nitrogen-Vacancy centers". In: *arXiv preprint arXiv:2206.06734* (2022).

[35] Zhecheng Wang et al. "Picotesla magnetometry of microwave fields with diamond sensors". In: *arXiv preprint arXiv:2206.08533* (2022).

[36] Scott T Alsid et al. "A Solid-State Microwave Magnetometer with Picotesla-Level Sensitivity". In: *arXiv preprint arXiv:2206.15440* (2022).

[37] L Rondin et al. "Nanoscale magnetic field mapping with a single spin scanning probe magnetometer". In: *Applied Physics Letters* 100.15 (2012), p. 153118.

[38] JP Tetienne et al. "Magnetic-field-dependent photodynamics of single NV defects in diamond: an application to qualitative all-optical magnetic imaging". In: *New Journal of Physics* 14.10 (2012), p. 103033.

[39] Robert Chapman and Taras Plakhoitnik. "Background-free imaging of luminescent nanodiamonds using external magnetic field for contrast enhancement". In: *Optics Letters* 38.11 (2013), pp. 1847–1849.

[40] Zachary R Jones et al. "Selective imaging of diamond nanoparticles within complex matrices using magnetically induced fluorescence contrast". In: *Environmental Science: Nano* 7.2 (2020), pp. 525–534.

[41] S Kolkowitz et al. "Probing Johnson noise and ballistic transport in normal metals with a single-spin qubit". In: *Science* 347.6226 (2015), pp. 1129–1132.

[42] Trond I Andersen et al. "Electron-phonon instability in graphene revealed by global and local noise probes". In: *Science* 364.6436 (2019), pp. 154–157.

[43] Aurore Finco et al. "Imaging non-collinear antiferromagnetic textures via single spin relaxometry". In: *Nature communications* 12.1 (2021), pp. 1–6.

[44] Georg Kucsko et al. "Nanometre-scale thermometry in a living cell". In: *Nature* 500.7460 (2013), pp. 54–58.

[45] Hengyun Zhou et al. "Quantum metrology with strongly interacting spin systems". In: *Physical review X* 10.3 (2020), p. 031003.

[46] D Le Sage et al. "Efficient photon detection from color centers in a diamond optical waveguide". In: *Physical Review B* 85.12 (2012), p. 121202.

[47] Edlyn V Levine et al. "Principles and techniques of the quantum diamond microscope". In: *Nanophotonics* 8.11 (2019), pp. 1945–1973.

[48] SC Scholten et al. "Widefield quantum microscopy with nitrogen-vacancy centers in diamond: Strengths, limitations, and prospects". In: *Journal of Applied Physics* 130.15 (2021), p. 150902.

[49] David R Glenn et al. "Micrometer-scale magnetic imaging of geological samples using a quantum diamond microscope". In: *Geochemistry, Geophysics, Geosystems* 18.8 (2017), pp. 3254–3267.

[50] Olivier Arcizet et al. "A single nitrogen-vacancy defect coupled to a nanomechanical oscillator". In: *Nature Physics* 7.11 (2011), pp. 879–883.

[51] Daniel Rugar et al. "Single spin detection by magnetic resonance force microscopy". In: *Nature* 430.6997 (2004), pp. 329–332.

[52] William S Huxter et al. "Scanning gradiometry with a single spin quantum magnetometer". In: *arXiv preprint arXiv:2202.09130* (2022).

[53] Joonhee Choi et al. "Depolarization dynamics in a strongly interacting solid-state spin ensemble". In: *Physical review letters* 118.9 (2017), p. 093601.

[54] Xi Feng et al. "Association of nanodiamond rotation dynamics with cell activities by translation-rotation tracking". In: *Nano letters* 21.8 (2021), pp. 3393–3400.